Journal of Building Engineering 100 (2025) 111791

Contents lists available at ScienceDirect

Journal of Building Engineering

journal homepage: www.elsevier.com/locate/jobe

Transformation function-based modal identification of superstructure of base-isolated buildings using responses of isolation layer

Kangqian Xu [a], Miao Cao [b], Songtao Xue [b,c], Xianzhi Li [a], Jigang Zhang [a], Zhuoran Yi [c,*], Liyu Xie [c]

[a] School of Civil Engineering, Qingdao University of Technology, Qingdao, China
[b] Department of Architecture, Tohoku Institute of Technology, Sendai, Japan
[c] Department of Disaster Mitigation for Structures, Tongji University, Shanghai, China

ARTICLE INFO

Keywords:
Base-isolated structure
Modal identification
Transformation function
Simple monitoring system
Real-life building

ABSTRACT

For a comprehensive diagnosis of base-isolated buildings, the superstructure should be monitored. The modal parameters are crucial evidence for structural assessment. This paper develops a novel method to identify the natural frequency of the superstructure using a transformation function that depends on the responses of the isolation story, eliminating the need for sensors installation in the superstructure. The transformation function of the isolation layer is defined as the ratio of the inter-story drift to the absolute acceleration of the story. The formulation is initially derived under linear conditions through a substructural approach, and it is extended to a nonlinear case using a generalized frequency response function. This function can identify the modal parameters of the superstructure. Numerical simulations of a base-isolated structure are performed to investigate the influence of nonlinearity. The method is validated using three real-world structures: (i) a scaled structure in a laboratory under linear conditions; (ii) a full-scale reinforced concrete (RC) structure with sliding bearings (tested at E-Defense); and (iii) a real-life base-isolated building equipped with bearings and dampers. Subspace identification (SI) is used for comparison. The results confirm that all the modes can be accurately estimated for a linear structure. When the isolation system behaves nonlinearly, the position of the poles of the superstructure is not affected, and the first two modes are identified, whereas the poles corresponding to higher modes cannot be observed. Hence, the natural frequencies of the first two modes extracted using the proposed approach are accurate and consistent with the SI results.

1. Introduction

Installing base isolation bearings in buildings can reduce structural damage during an earthquake. This seismic isolation system can alter a structure's first natural frequency from the dominant frequency of the seismic load, thereby reducing the building's structural responses [1,2]. Moreover, the inter-story drift of the isolation story should be measured by displacement sensors [3] or emerging measurement techniques [4,5] to assess whether the isolation system is effective under external forces, as a large displacement may

* Corresponding author.
E-mail address: yzr1997@tongji.edu.cn (Z. Yi).

https://doi.org/10.1016/j.jobe.2025.111791
Received 7 December 2024; Received in revised form 31 December 2024; Accepted 4 January 2025
Available online 7 January 2025

disable the bearings and dampers [6–9]. Despite the utilization of the seismic isolation and the incorporation of the supplemental passive [10–12], semi-active [13,14], or active energy dissipation devices [15,16], the superstructure vibrates due to ground motion and could be damaged during a strong earthquake [17,18]. Hence, monitoring the superstructure of seismically isolated buildings is necessary.

Structural diagnosis based on responses recorded by monitoring system is convenient, with various types of evidence extracted from the structural responses for assessment [19–21]. For this reason, characteristics such as modal parameters are very suitable since they are directly related to structural properties [22]. Generally, a monitoring system is composed of sensors and the associated data acquisition, transmission, and processing devices [23]. Wired data transmission still is a common practice, and an autonomous wiring arrangement allows for the proper functioning of the sensing system for extreme events [24]. However, the installation and maintenance of these sensors on multiple floors is tedious and expensive. Therefore, in this work the use of a simplified sensing system for the modal identification of the superstructure in a base-isolated building is investigated.

To date, the modal identification of base-isolated structures has been extensively studied [25–29]. High damping bearings with supplemental dampers are typically employed for energy dissipation and shock absorption, as the use of the elastomeric isolator alone will increase base displacement [30,31]. As a result, the behavior of the isolation layers becomes nonlinear. In such cases, modal information can be identified by considering the whole building as a system, where the seismic wave is the input and the responses of the base and floors are the output; the following two components of this system are obtained: (i) the characteristics of the isolation system; and (ii) the dynamic properties related to the superstructure [32,33]. However, these two components are coupled to each other, making it difficult to determine the state of the superstructure from these modal parameters. For example, the natural frequency of the superstructure is different under earthquakes of different intensities; consequently, identifying whether the change originated from the nonlinearity of the bearings and dampers or from structural damage is challenging.

A fixed-base structure system model can be used to make an accurate structural estimation of a superstructure [18,34]. In this model, the response of the base is the system input, whereas the responses of the other stories are the system output. However, the absolute responses cannot be directly used for output-only methods because the hysteretic information of the isolation system has not been disaggregated from the superstructure responses. This suggests that the sensors deployed on the base and the floors of the superstructure are required. A building can experience diverse damage modes [35,36]. In the event of significant time-varying characteristics, extended Kalman filters [37–39] and unscented Kalman filters [40–42] can be used to track the varying structural parameters. The Kalman-type algorithms require structural mass distribution, and a rough mass estimate will not provide accurate results. In contrast, time-frequency domain analyses, such as the Hilbert-Huang transform [43,44] and the wavelet transform [45,46], do not require the structural mass data and can reflect varying structural information, if floor responses relative to the base can be obtained. Furthermore, a combination of a short-time transfer function and a subspace identification (SI) method is presented to improve the accuracy of the identification of the natural frequency of a superstructure [18]. However, time-domain and frequency-domain time-invariant identification studies (e.g., the transmissibility function) of full-scale buildings and real-life structures, which use the time-history responses of common structural damage to buildings, can afford satisfactory results [32,47–50]. For example, the natural frequency identified by the time-invariant identification method will decrease when the extent of the structural damage increases for common buildings. Therefore, the time-invariant identification method can provide a reliable assessment of the structural condition with higher identification accuracy and operational convenience. However, the aforementioned identification methods require both the structural responses of the base and superstructure. For this, sensors must be installed on the superstructure in addition to the base. In particular, a sufficient number of sensors must be distributed in a superstructure with multiple floors to ensure a high identification accuracy [51]. This could increase the cost of the structural monitoring system.

To address the abovementioned issues, this paper focuses on the modal identification of a superstructure using a simple monitoring system. This method requires only the measured absolute acceleration and inter-story displacement of the isolation layer. A substructural approach is used to derive a linear transformation function of the isolation story, which is defined as the ratio of the inter-story drift to the absolute acceleration. Subsequently, a generalized frequency response function is adopted to extend the transformation function to nonlinear conditions. This transformation function is used for the modal identification of the superstructure. As mentioned before, the isolation system has to be monitored with an accelerometer and displacement meter that are mounted at the base. The proposed method makes full use of the responses collected by the two sensors and requires no additional sensors for the superstructure. The two sensors, along with other equipment, can be placed in a single location within the seismic isolation building, which reduces the wiring requirements and minimizes spatial waste, thus significantly lowering monitoring costs.

The reset of this paper is organized as follows: Section 2 describes the development of the transformation function for modal identification under linear and nonlinear conditions. Section 3 discusses the influence of the degree of nonlinearity on the transformation function-based modal identification through numerical simulations. Section 4 presents the validation results of the proposed algorithm when it was applied to a scaled steel structure in the laboratory, a full-scale reinforced concrete (RC) structure with sliding bearings (tested at E-Defense, a part of the Japan's National Research Institute for Earth Science and Disaster Resilience), and a real-life base-isolated building with nonlinear bearings and dampers. Different column sizes are investigated in the first case, and seismic waves with multiple intensities are applied to the latter two cases. Finally, Section 5 summarizes our findings and discusses the potential applications of the proposed method.

2. Methodology

A schematic of the motion of a base-isolated structure is shown in Fig. 1. The equation of motion of the whole structure subjected to earthquakes can be expressed as follows:

$$\mathbf{M}\ddot{\mathbf{z}}(t) + \mathbf{C}\dot{\mathbf{z}}(t) + \mathbf{K}\mathbf{z}(t) = -\mathbf{M}\mathbf{r}\ddot{u}_g(t) \tag{1}$$

where **M**, **C**, and **K** are the mass, damping, and stiffness matrices that consists of $[m_b \quad m_1 \quad \cdots \quad m_n]$, $[c_b \quad c_1 \quad \cdots \quad c_n]$, and $[k_b \quad k_1 \quad \cdots \quad k_n]$, respectively; $\mathbf{z}(t)$ is the response relative to the ground; $(\dot{\cdot})$ is the time derivative; $\ddot{u}_g$ is the seismic acceleration; and $\mathbf{r}$ is an all-one vector.

To propose a modal identification method for the superstructure of the base-isolated structures based solely on the absolute acceleration and inter-story drift of the isolation layer, the linear case is investigated first as an initial study. This is followed by an investigation of a general nonlinear condition.

2.1. Linear condition: analysis of whole structure

In this section, suppose that the isolation layer behaves linearly during earthquakes. Then, Equation (1) can be expressed in the frequency domain as follows:

$$\mathbf{Z}(\omega) = \mathbf{H}^{\mathrm{dis}}_{whole}(\omega)\mathbf{M}^{\mathrm{vector}}\ddot{U}_g(\omega) \tag{2-1}$$

$$\dot{\mathbf{Z}}(\omega) = \mathbf{H}^{\mathrm{vel}}_{whole}(\omega)\mathbf{M}^{\mathrm{vector}}\ddot{U}_g(\omega) \tag{2-2}$$

$$\ddot{\mathbf{Z}}(\omega) = \mathbf{H}^{\mathrm{acc}}_{whole}(\omega)\mathbf{M}^{\mathrm{vector}}\ddot{U}_g(\omega) \tag{2–3}$$

$$\mathbf{M}^{\mathrm{vector}} = [-m_b \quad -m_1 \quad \cdots \quad -m_n]^{\mathrm{T}}$$

$$\mathbf{H}^{\mathrm{dis}}_{whole}(\omega) = \frac{1}{j\omega}\mathbf{H}^{\mathrm{vel}}_{whole}(\omega) = -\frac{1}{\omega^2}\mathbf{H}^{\mathrm{acc}}_{whole}(\omega)$$

$$\mathbf{H}^{\mathrm{dis}}_{whole}(\omega) = \begin{bmatrix} H_{bb}(\omega) & H_{b1}(\omega) & \cdots & H_{bi}(\omega) & \cdots & H_{bn}(\omega) \\ H_{1b}(\omega) & H_{11}(\omega) & \cdots & H_{1i}(\omega) & \cdots & H_{1n}(\omega) \\ \vdots & \vdots & \ddots & \vdots & \ddots & \vdots \\ H_{ib}(\omega) & H_{i1}(\omega) & \cdots & H_{ii}(\omega) & \cdots & H_{in}(\omega) \\ \vdots & \vdots & \ddots & \vdots & \ddots & \vdots \\ H_{nb}(\omega) & H_{n1}(\omega) & \cdots & H_{ni}(\omega) & \cdots & H_{nn}(\omega) \end{bmatrix}$$
$$= \begin{bmatrix} -\omega^2 m_b + (k_b + k_1) + j\omega(c_b + c_1) & -k_1 - j\omega c_1 & 0 \\ & \ddots & \\ 0 & & -\omega^2 m_n + k_n + j\omega c_n \end{bmatrix}^{-1}$$

where $\mathbf{Z}(\omega)$ and $\ddot{U}(\omega)$ are the Fourier transforms of $\mathbf{z}(t)$ and $\ddot{u}(t)$, respectively; $\mathbf{H}^{\mathrm{dis}}_{whole}(\omega)$, $\mathbf{H}^{\mathrm{vel}}_{whole}(\omega)$, and $\mathbf{H}^{\mathrm{acc}}_{whole}(\omega)$ are the displacement, velocity, and acceleration frequency response function, respectively, of the whole building; and j is the imaginary unit.

The inter-story drift $Z_b(\omega)$ of the isolation layer is described as follows:

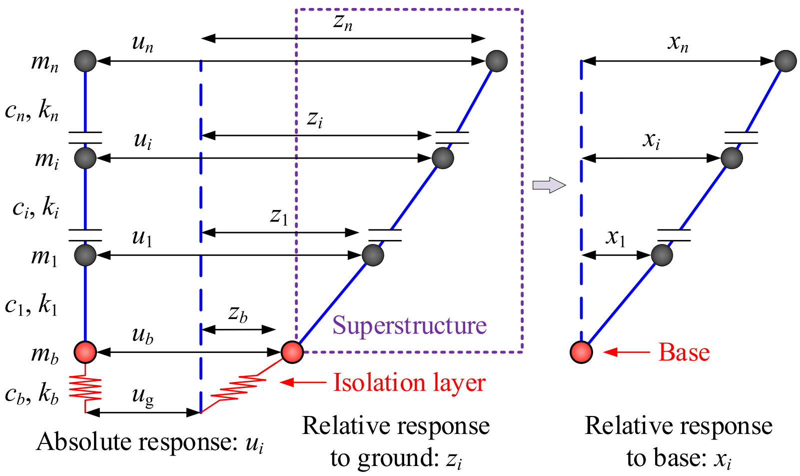

Fig. 1. Schematic of the motion of a base-isolated building.

$$Z_b(\omega) = [-m_bH_{bb}(\omega) - m_1H_{b1}(\omega) - \cdots - m_iH_{bi}(\omega) - \cdots - m_nH_{bn}(\omega)]\ddot{U}_g(\omega) \tag{3}$$

The absolute acceleration $U_b(\omega)$ of the base can be written as follows:

$$U_b(\omega) = -\omega^2[-m_bH_{bb}(\omega) - m_1H_{b1}(\omega) - \cdots - m_iH_{bi}(\omega) - \cdots - m_nH_{bn}(\omega)]\ddot{U}_g(\omega) + \ddot{U}_g(\omega) \tag{4}$$

Consequently, the ratio of the inter-story displacement to the absolute acceleration of the isolation story can be expressed in the frequency domain as follows:

$$\frac{Z_b(\omega)}{U_b(\omega)} = \frac{[-m_bH_{bb}(\omega) - m_1H_{b1}(\omega) - \cdots - m_iH_{bi}(\omega) - \cdots - m_nH_{bn}(\omega)]}{-\omega^2[-m_bH_{bb}(\omega) - m_1H_{b1}(\omega) - \cdots - m_iH_{bi}(\omega) - \cdots - m_nH_{bn}(\omega)] + 1} \tag{5}$$

2.2. Simplified formulation: substructural analysis

Equation (5) affords the response analysis of the whole structure. However, interpreting this complex expression is difficult. Therefore, a substructural analysis is applied to simplify the formulation [52]. The equation of the motion of the superstructure is given as follows:

$$\mathbf{M}_s\ddot{\mathbf{x}}(t) + \mathbf{C}_s\dot{\mathbf{x}}(t) + \mathbf{K}_s\mathbf{x}(t) = -\mathbf{M}_s\mathbf{r}\ddot{u}_b(t) \tag{6}$$

The equation of motion for the structural base is expressed as follows:

$$m_b\ddot{z}_b(t) + c_b\dot{z}_b(t) + k_bz(t) = -m_b\ddot{u}_g(t) + f_{sup}(t) \tag{7}$$

where the subscript ‘s’ indicates the matrices of the superstructure that are composed of $[m_1 \ \cdots \ m_n]$, $[c_1 \ \cdots \ c_n]$, and $[k_1 \ \cdots \ k_n]$; $\mathbf{x}(t)$ is the response relative to the base; $\ddot{u}_b$ is the absolute acceleration of the base, and $f_{sup}(t)$ is the force exerted by the superstructure.

Similar to Equation (1), which describes the whole structure, Equation (6) describes the superstructure and can be expressed in the frequency domain as follows:

$$\mathbf{X}(\omega) = \mathbf{H}_{sup}^{\mathrm{dis}}(\omega)\mathbf{M}_{sup}^{\mathrm{vector}}\ddot{U}_b(\omega) \tag{8-1}$$

$$\dot{\mathbf{X}}(\omega) = \mathbf{H}_{sup}^{\mathrm{vel}}(\omega)\mathbf{M}_{sup}^{\mathrm{vector}}\ddot{U}_b(\omega) \tag{8-2}$$

$$\ddot{\mathbf{X}}(\omega) = \mathbf{H}_{sup}^{\mathrm{acc}}(\omega)\mathbf{M}_{sup}^{\mathrm{vector}}\ddot{U}_b(\omega) \tag{8-3}$$

$$\mathbf{X}(\omega) = [X_1(\omega) \ \cdots \ X_i(\omega) \ \cdots \ X_n(\omega)]^{\mathrm{T}}$$

$$\mathbf{M}_{sup}^{\mathrm{vector}} = [-m_1 \ \cdots \ -m_i \ \cdots \ -m_n]^{\mathrm{T}}$$

$$\mathbf{H}_{sup}^{\mathrm{dis}}(\omega) = \frac{1}{j\omega}\mathbf{H}_{sup}^{\mathrm{vel}}(\omega) = -\frac{1}{\omega^2}\mathbf{H}_{sup}^{\mathrm{acc}}(\omega)$$

$$\mathbf{H}_{sup}^{\mathrm{dis}}(\omega) = \begin{bmatrix} \overline{H}_{11}(\omega) & \cdots & \overline{H}_{1i}(\omega) & \cdots & \overline{H}_{1n}(\omega) \\ \vdots & \ddots & \vdots & \ddots & \vdots \\ \overline{H}_{i1}(\omega) & \cdots & \overline{H}_{ii}(\omega) & \cdots & \overline{H}_{in}(\omega) \\ \vdots & \ddots & \vdots & \ddots & \vdots \\ \overline{H}_{n1}(\omega) & \cdots & \overline{H}_{ni}(\omega) & \cdots & \overline{H}_{nn}(\omega) \end{bmatrix}$$
$$= \begin{bmatrix} -\omega^2m_1 + (k_1 + k_2) + j\omega(c_1 + c_2) & -k_2 - j\omega c_2 & 0 \\ & \ddots & \\ 0 & & -\omega^2m_n + k_n + j\omega c_n \end{bmatrix}^{-1}$$

where $X(\omega)$ is the Fourier transform of $x(t)$; $\mathbf{H}_{sup}^{\mathrm{dis}}(\omega)$, $\mathbf{H}_{sup}^{\mathrm{vel}}(\omega)$, and $\mathbf{H}_{sup}^{\mathrm{acc}}(\omega)$ are the frequency response functions of the superstructure; and $\overline{H}(\omega)$ is the element of $\mathbf{H}_{sup}^{\mathrm{dis}}(\omega)$.

Equation (7) characterizes the structural base and can be converted into the frequency domain as follows:

$$Y_b(\omega) = H_b(\omega)F_b(\omega) = H_b(\omega)\left[-m_b\ddot{U}_g(\omega) + F_{sup}(\omega)\right] \tag{9}$$

$$H_b(\omega) = \frac{1}{-\omega^2m_b + j\omega c_b + k_b}$$

$$F_b(\omega) = \Upsilon_{sup}(\omega)\ddot{U}_b(\omega)$$

$$\Upsilon_{sup}(\omega) = (j\omega c_{i+1} + k_{i+1})[-m_{i+1}\overline{H}_{(i+1)(i+1)}(\omega) - \cdots - m_n\overline{H}_{(i+1)n}(\omega)]$$

where $H_b(\omega)$ is the frequency response function of the base, $F_b(\omega)$ is the total force applied to the base, and $F_{sup}(\omega)$ is the Fourier transform of $f_{sup}(t)$.

Consequently, the transformation function $\Gamma_b(\omega)$, which is the ratio of the inter-story displacement to the absolute acceleration of the isolation story, can be formulated as follows:

$$\Gamma_b(\omega) = \frac{Y_b(\omega)}{U_b(\omega)} = \frac{-m_b + \Upsilon_{sup}(\omega)}{j\omega c_b + k_b} \tag{10}$$

$\overline{H}(\omega)$ is the element of the displacement frequency response function $\mathbf{H}_{sup}^{\mathrm{dis}}(\omega)$ of the superstructure. Hence, the modal characteristics of the superstructure are reflected by these elements. For example, those curves have peaks at the natural frequencies of the superstructure. Consequently, $\Upsilon_{sup}(\omega)$ is relevant only to the parameters of the superstructure and can indicate the modal information of the superstructure as well. Furthermore, the denominator of Equation (10) contains no zeros in the common frequency range and hence does not result in new poles. Thus, the transformation function $\Gamma_b(\omega)$ curve will have a similar feature to that of $\Upsilon_{sup}(\omega)$ in the numerator. In other words, the natural frequency of the superstructure can be determined from the transformation function through the peak-picking method.

2.3. *Extension to general case*

Isolation devices with nonlinear characteristics typically show superior energy dissipation and seismic mitigation performance. Hence, they are more frequently adopted in the isolation layer, which exhibits nonlinear behavior during major earthquakes. Assuming that the superstructure behaves linearly during the vibration. Previous studies [53–55] have presented the concept of a generalized frequency response function to describe nonlinearity, such as piecewise linearity and hysteresis nonlinearity, using a rational polynomial function, where the polynomial coefficients denote the nonlinear properties. For instance, when the stiffness nonlinearity is considered, the motion of the base can be expressed as follows:

$$m_b\ddot{z}_b(t) + c_b\dot{z}_b(t) + \sum_{p=1}^{P} k_{bj} z_b^p(t) = -m_b\ddot{u}_g(t) + f_{sup}(t) \tag{11}$$

where the subscript p is the order of nonlinearity.

Furthermore, as shown in Equation (12), the nonlinear inter-story drift of the isolation layer in the frequency domain can be divided into first-order and higher-order responses. The first-order response is the product of the frequency response function $H_b(\omega)$ of the base under linear conditions and the system input. The higher-order responses can be computed by the higher-order frequency response functions and the input. In particular, any higher-order frequency response function can be described as a polynomial function of the structural parameters.

$$Z_b(\omega) = H_b(\omega)F_b(\omega) + \sum_{p=2}^{P} \mathrm{func}_p\left(\omega, m_b, c_b, k_{b1}, \cdots, k_{bp}, H_b(\omega), F_b(\omega)\right) \tag{12}$$

where func(·) denotes the functional relationship.

The expression of the transformation function of a nonlinear isolation layer can be approximately obtained by substituting Equation (9) for Equation (12):

$$\Gamma_b(\omega) = \frac{Z_b(\omega)}{U_b(\omega)} \doteq \frac{-m_b + \Upsilon_{sup}(\omega)}{j\omega c_b + k_b + \mathrm{func}\left(\omega, m_b, c_b, k_{b1}, \cdots, k_{bp}, \cdots k_{bp}\right)} \tag{13}$$

The denominator of Equation (13) contains two components: (i) the first two terms are the same as those in the linear case, and (ii) the function term associated with nonlinearity. The contribution of the nonlinear term is significantly smaller than that of the linear part. Therefore, the denominator does not undergo a sign change within the frequency range of interest. Hence, the poles of the transformation function are consistent with those of $\Upsilon_{sup}(\omega)$. Even when the stiffness and damping nonlinearity of the isolation system are considered simultaneously, the result remains the same.

Notably, for a nonlinear single-degree-of-freedom (SDOF) structure, additional poles appear except for that of the natural frequency in the linear case. In contrast, no extra poles appear in the transformation function because the term $-\omega^2 m_b$ in the denominator is eliminated. In addition, according to Equation (10), under linear conditions, the transformation function of the isolation layer will remain constant when the structure is excited by different seismic waves. However, under nonlinear conditions, the amplitude of the transformation function will differ at the same frequency, as the nonlinear parameters reflected by the polynomial coefficients will vary under different loads. In summary, the natural frequency of the superstructure can be determined from the transformation function of the isolation layer, i.e., the ratio of the inter-story drift to the absolute acceleration, and the identification process is illustrated in Fig. 2. Therefore, the superstructure can be monitored by an accelerometer and a displacement sensor installed on the isolation story.

3. Numerical simulations

To investigate the influence of the nonlinearity of the isolation layer on the modal identification of the superstructure using the transformation function, simulations on a three-story base-isolated shear structure were conducted. The lumped mass and the inter-story stiffness of the superstructure and the base are shown in Fig. 3. The widely used Bouc-Wen hysteresis model [56,57] was adopted to simulate the hysteresis of the energy dissipation and seismic isolation devices. Even though this model does not fully align with the plasticity theory and may occasionally predict negative energy dissipation, it is widely applied in the seismic engineering field. The equation governing the Bouc-Wen model is expressed as follows:

$$D_y\dot{w} = A\dot{u}_b - (\gamma \mathrm{sgn}(w\dot{u}_b) + \beta)|w|^n\dot{u}_b \tag{14}$$

The hysteretic force F_{bh} of the isolation story can be obtained by the following equation:

$$F_{bh} = F_y w \tag{15}$$

where w is a dimensionless hysteretic variable, and D_y and F_y are the yield displacement of the energy dissipation and seismic isolation equipment, respectively. In this simulation, we used a D_y of 1.5 mm and an F_y of 655.4 kN. A, β, γ, and n characterize the shape of the hysteresis loop and were set to 0.0029, 0.6, 0.4, and 1.0, respectively.

Gaussian white noise signals with different amplitudes (1 %, 10 %, 25 %, 50 %, 75 %, and 100 %) were used to excite the base-isolated structure. The hysteretic force inter-story displacement curves of the isolation story are shown in Fig. 4. When the structure was subjected to the load with 1 % amplitude, it behaved linearly because of the minor excitation. The device exhibited varying extents of nonlinearity as the amplitude of the load increased. The transformation function of the isolation layer can be determined by the absolute acceleration and the inter-story drift of the isolated story. Fig. 5 shows the transformation function of the isolation layer under all situations. In all the cases, the pole corresponding to the first mode was significant, and the second pole was small yet noticeable. However, the higher modes did not appear because the contribution of nonlinearity becomes comparable to, or even larger than, that of the linear part in the denominator of Equation (13) as the frequency increases. Consequently, the original poles of the higher-order modes are obscured by nonlinearity-induced fluctuations. In addition, the amplitudes of the transformation function are different under different excitations. For example, the values of the function became larger near the first peak. This implies that, in the denominator of Equation (13), the nonlinear term has the opposite sign to that of the linear term, and its magnitude increased as the hysteresis loop became more pronounced. Furthermore, the natural frequencies of the first two modes of the superstructure were extracted from the function curves, and the errors relative to the analytic values were computed. These results are listed in Table 1. As can be observed, the first two natural frequencies of the superstructure were accurately identified by the transformation function, and the identification of these parameters were not affected by the nonlinearity. In summary, the nonlinearity of the isolation layer influenced the amplitude of the transformation function but did not affect the position of the poles. This nonlinearity also results in the inability to observe the poles corresponding to the higher modes (≥3) in the function curve.

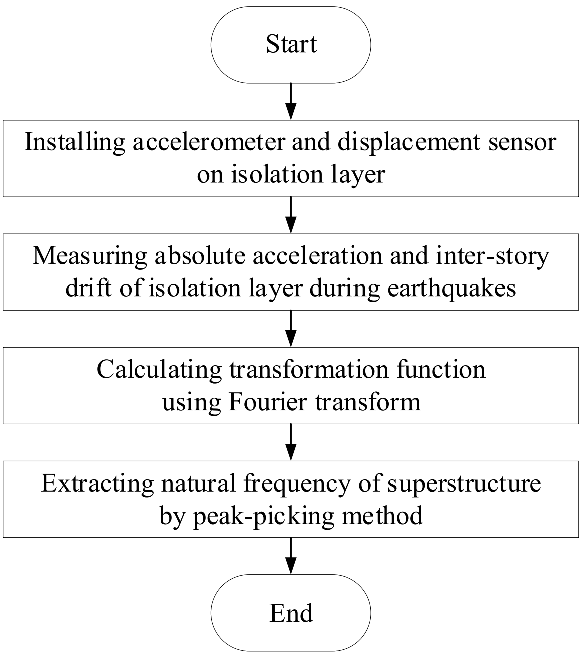

Fig. 2. Procedure of modal identification by the transformation function.

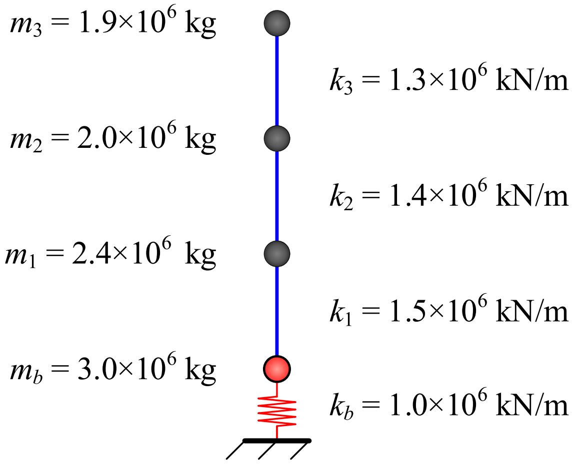

Fig. 3. Three-story base-isolated structure.

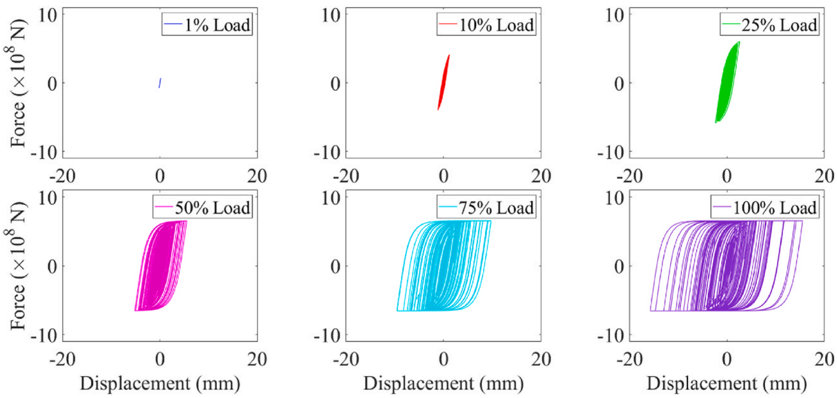

Fig. 4. Hysteresis loops of the isolation layer under loads with different amplitudes.

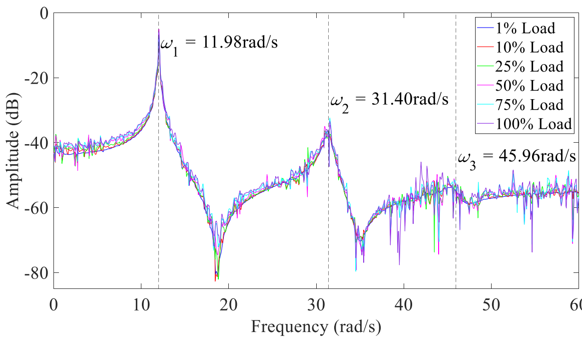

Fig. 5. Transformation function of the isolation layer under loads with different amplitudes.

4. Validation

Three scenarios were used to validate the applicability of the transformation function of the isolation layer for the modal identification of the superstructure. In Section 4.1, the application of the transformation function to a scaled steel frame in laboratory under linear conditions is discussed. Section 4.2 describes the application of the proposed algorithm to a full-scale RC structure tested at E-Defense, where cast iron supports were used at the base. In Section 4.3, the responses of a real-life building under two earthquakes with different intensities are used. In particular, the isolation layer of the building was equipped with rubber bearings and oil dampers. For

Table 1
Identified parameters of the superstructure and relative errors to the analytic values
(Analytic value: First natural frequency = 11.99 rad/s; second natural frequency = 31.40 rad/s).

Amplitude of loads	First natural frequency (rad/s)	Relative error (%)	Second natural frequency (rad/s)	Relative error (%)
1 %	12.03	0.34	31.37	0.10
10 %	12.03	0.34	31.37	0.10
25 %	12.03	0.34	31.37	0.10
50 %	12.03	0.34	31.55	0.47
75 %	12.03	0.34	31.55	0.47
100 %	12.03	0.34	31.55	0.47

comparison, the subspace identification (SI) [58] was applied to identify the natural frequency in all three cases. Finally, the results are discussed in Section 4.4.

4.1. Laboratory experiment: linear case

The proposed identification method was applied to recognize the modal parameters to a scaled structure in a linear case. As shown in Fig. 6(a), this scaled structure had five floors. Assuming that the first story is an isolation layer that is composed of linear members. Thus, the first floor was considered the base, and the superstructure was considered a four-degree-of-freedom (four-DOF) structure. The bronze columns had dimensions of $0.0025 \times 0.03 \times 0.24\ \mathrm{m}^3$ and a Young's modulus of $1 \times 10^{11}\ \mathrm{N/m}^2$, which resulted in an inter-story stiffness of $1.3563 \times 10^4\ \mathrm{N/m}$. The structure was excited using a conventional electrodynamic vibrator. SS-1 model accelerometers (Tokyo Sokushin) were used to capture the structural responses of the isolation story and superstructure. The inter-story drift of the isolation layer was calculated from the acceleration responses measured from the top and bottom of the story.

A sinusoidal sweep wave was used to vibrate the scaled structure. The transformation function of the isolation layer can be determined by the recorded absolute acceleration and the computed inter-story displacement, as plotted in Fig. 7(a). The poles correspond to the natural frequencies of the superstructure. Notably, the anti-resonance frequencies in the transformation function are solely related to the parameters of the superstructure. However, they are not identical to the anti-resonance frequencies observed in the superstructure's frequency response function. The For comparison, the SI was employed to identify the natural frequency of the superstructure. The acceleration responses of the superstructure (from the second to the fifth floors) were considered the output, and the absolute acceleration of the top of the isolation story (the first floor) was considered the input. To obtain a reliable estimation, the parameters was identified using different model orders, from $2n_{\mathrm{sup}}$ to 60 at steps of 2, where n_{sup} is the number of the DOF of the superstructure. The most similar parameters between two adjacent model orders were considered valid parameters. For each mode, the valid parameters identified across all model orders were averaged after excluding any outliers to obtain the natural frequency corresponding to that mode. The valid parameters are shown as red solid circles in Fig. 7(a). Intuitively, the natural frequencies were accurately identified under different model orders and were consistent with the poles of the transformation function. The natural frequencies of the first, second, third, and fourth modes identified by the SI were 19.1, 60.3, 92.4, and 113.9 rad/s, respectively. The peak-picking method was used to determine the natural frequencies from the transformation function, relative errors in the two approaches of the SI and the transformation function were computed, as shown in the top panel of Fig. 8. The modal identification by the

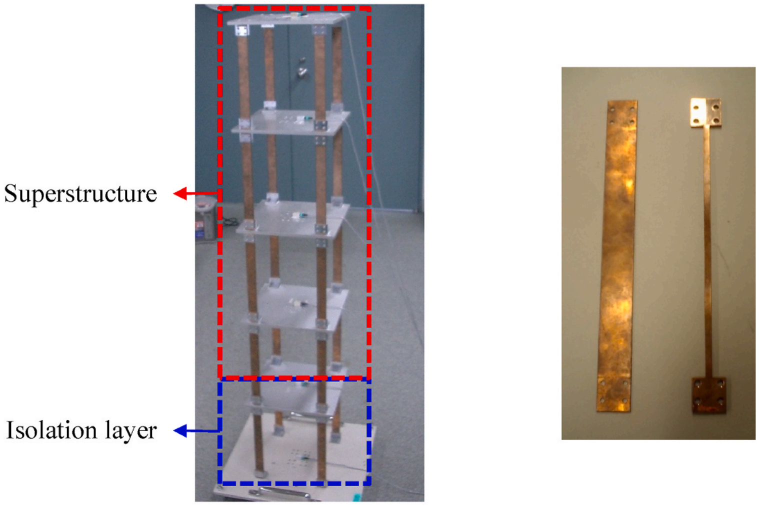

(a) Scaled structure (b) Original (left) and weak (right) column

Fig. 6. Experimental setup.

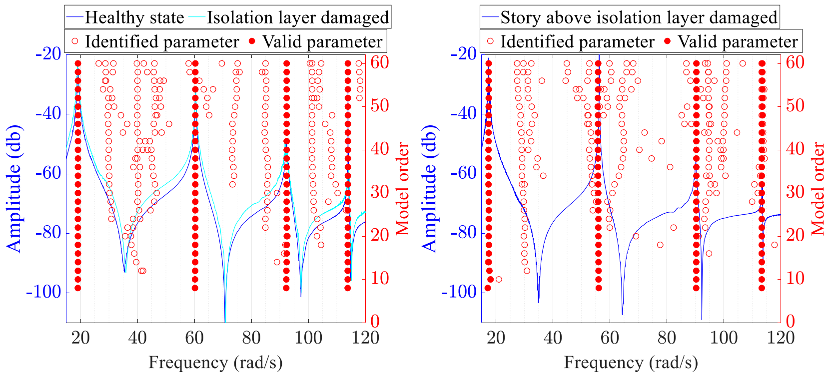

Fig. 7. Transformation function of the isolation layer and natural frequencies identified by SI (Note: Curve in figures is transformation function).

proposed approach was consistent with that of the SI owing to the recognizable acute peak in the function curve.

As shown in Fig. 6(b), a column with a small size of $0.003 \times 0.006 \times 0.24$ m^3 was used to simulate the structural damage. In the first case, two original columns of the isolation layer were substituted by the weak columns, and the superstructure remained intact. In theory, the modal parameters of the superstructure will not be affected. The damaged structure was excited, and the transformation function of the isolation layer was determined by the recorded responses of this story (the turquoise curve in Fig. 7(a)). The transformation function underwent only a vertical shift when the stiffness of the isolation layer decreased, while the location of the poles remained unchanged. In the second case, the columns of the bottom story of the superstructure were replaced, imitating the damage to the superstructure. Similarly, the SI was applied to extract the eigenvalues from the measured absolute responses. The identified data and the valid parameters are shown in Fig. 7(b). The average values of the first, second, third, and fourth natural frequencies were 17.4, 55.9, 90.4, and 113.3 rad/s, respectively, which exhibit a decreasing tendency as the inter-story stiffness decreased. The transformation function was computed using the absolute acceleration and the inter-story drift of the isolation story. Compared to the curves in Fig. 7(a), the transformation function in Fig. 7(b) shifted to the left owing to the changed parameters in the superstructure. The overlap of the poles of the function curves is evident with the frequency points identified by the SI. In particular, as shown in the bottom panel of Fig. 8, the natural frequencies extracted from the curve by the peak-picking method have minor errors compared with the parameters identified by the SI. In summary, for a linearly vibrating structure, the poles corresponding to all modes of the superstructure were obvious, and all the natural frequencies of the superstructure were accurately determined from the transformation function.

4.2. E-Defense test

The proposed algorithm was applied to a full-scale RC structure. The data was obtained from E-Defense Experimental Data Archive (ASEBI). The structure was tested at E-Defense as part of the project titled “Experimental Study on Collapse Mechanism of 10-story RC Frame Based on Current Seismic Design Code and Advanced High Seismic Technology”. As shown in Fig. 9(a), the superstructure had 10 stories, and the dimensions of the floor were 13.5 m in the long direction (Y direction) and 9.5 m in the short direction (X direction). The heights of the first, second-to-fourth, fifth-to-seventh, and eighth-to-tenth stories were 2.8, 2.6, 2.55, and 2.5 m, respectively. The frame structure was along the Y direction and had dimensions of 4.0 m $\times$ 3. To reduce the external forces acting on the superstructure during earthquakes, 16 cast iron supports were used between the bottom concrete and the base of the superstructure (Fig. 9(b)). The cast iron supports were 40 mm thick, out of which 20 mm was embedded in the bottom concrete. When the superstructure was placed on the cast iron supports, they are expected to function as sliding supports. TA-25E accelerometers (Tokyo Keiki) and displacement

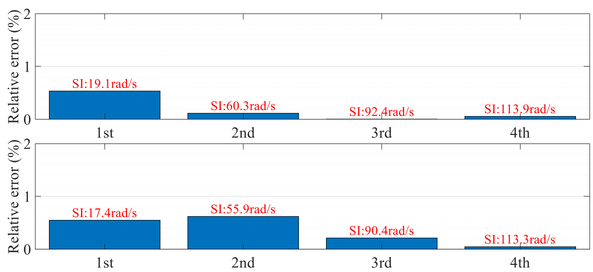

Fig. 8. Relative errors of natural frequencies identified by the transformation function and SI (Top part: Superstructure is healthy; Bottom part: Superstructure is damaged).

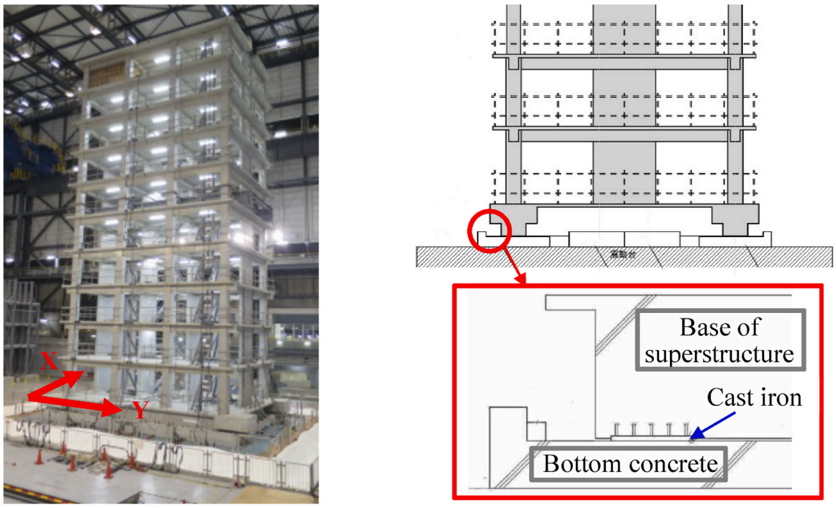

(a) Photograph of a full-scale structure (b) Section view of the structural base

Fig. 9. Shaking table test of a ten-story RC frame.

sensors were placed on a shaking table, the bottom concrete, and the base and all floors of the superstructure to record the structural responses. Both potentiometer- and laser-type displacement sensors were used to provide distinct measurement ranges and precision levels, which would afford more accurate displacement data. In this study, the responses along the Y direction were focused on.

First, a Gaussian white noise with a root-mean-square of 0.075 m/s^2 was used to excite the structure. Then, the JMA Kobe earthquake waves (NS component) with amplitudes of 25 %, 50 %, and 100 % were applied sequentially. The time-history and normalized power spectral density of the external loads are shown in Fig. 10. The measured inter-story drift of the isolation layer is plotted in Fig. 11(a). No foundation slip under the excitation of the white noise was observed. However, as the amplitude of the seismic loads increased from 25 % to 50 %, the foundation slip increased from approximate 50 mm–160 mm. At a 100 % amplitude, the vibrational amplitude of the inter-story drift increased but the final sliding displacement decreased. Furthermore, the restoring force of the first story of the superstructure was employed to reflect the structural state. The restoring force consists of two components: the rigid inertial force of the superstructure and the inertial force of the lumped floors [34]. The floor mass was obtained from the experimental report, and the acceleration responses of all the floors were measured. Then, the restoring forces in the four excitation cases were computed (Fig. 11(b)). The superstructure behavior was linear under white noise. A slight hysteresis appeared at 25 % seismic excitation. The nonlinear behavior intensified as the load amplitude increased. Correspondingly, the column and the beam-column joint damage at the first story of the superstructure had been observed, and the results of restoring force correlated well with these observations.

The SI was applied to determine the natural frequency of the superstructure at 50 % seismic excitation. The absolute acceleration of the base of the superstructure was the system input, whereas the recorded responses of all 10 floors were the system output. The parameters were extracted under model orders from 20 to 60, as shown in Fig. 12(a). In the 0–120 rad/s frequency range, the natural frequencies of the first six modes are listed in Table 2. The standard deviations for the valid parameters of the first two modes under different model orders were small, indicating their reliability. To investigate the influence of the number of outputs on the SI, the

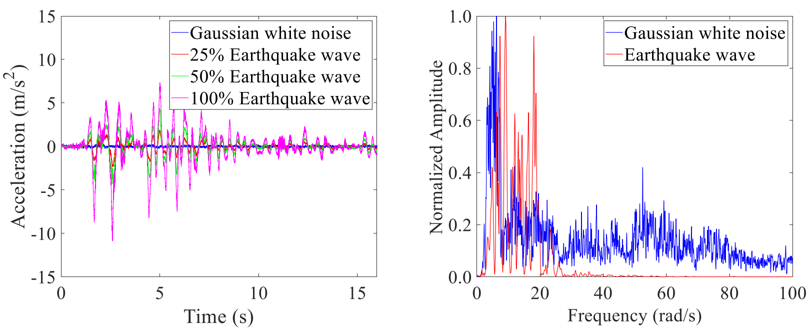

(a) Time history (b) Normalized power spectral density

Fig. 10. External excitation.

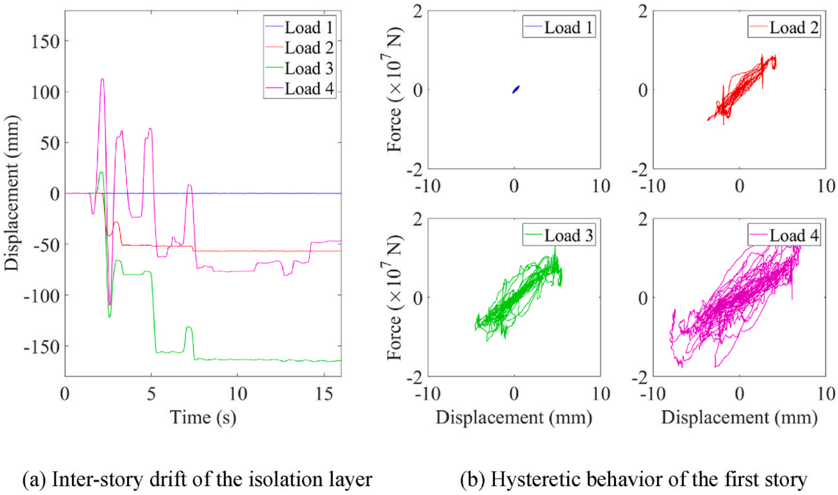

Fig. 11. Structural behavior under different excitations (Load 1: Gaussian white noise; Load 2: 25 % earthquake wave; Load 3: 50 % earthquake wave; Load 4: 100 % earthquake wave).

modal parameters were determined considering only the absolute acceleration responses of the fifth and top floors as the system output. As displayed in Fig. 12(b), the parameters identified using two sensors were comparable to those obtained using ten accelerometers; however, the standard deviations of the valid parameters estimated using two sensors became larger for higher modes, indicating the unreliability of this data. Furthermore, the transformation function was computed using the recorded absolute acceleration and inter-story drift of the isolation layer (Fig. 12). The pole corresponding to the first mode was sharp, whereas that associated with the second mode was less pronounced. The curve peaks exhibited visual correlation with the valid parameters obtained from the SI. In addition, the extraction of information regarding higher modes from the transformation function is extremely difficult. The natural frequencies of the first two modes identified from the transformation function were 7.62 and 26.27 rad/s, respectively. The relative errors of the parameters obtained by the SI and the transformation function were 1.94 % and 0.75 %, respectively. These results are also listed in Table 2. This indicates that the proposed algorithm afforded accurate modal identification, regardless of the nonlinear behavior of the superstructure.

The transformation functions of the isolation layer under four different excitations were calculated (Fig. 13). In the case of the Gaussian white noise, the second mode was difficult to extract, likely because of the minor amplitude of the load. The natural frequencies of the first mode subjected to white noise and 25 %, 50 %, and 100 % earthquake waves were 8.71, 8.50, 7.62, and 7.04 rad/s, respectively. The identified parameters of the second mode subjected to 25 %, 50 %, and 100 % earthquake waves were 28.73, 27.27, and 23.47 rad/s, respectively. The first natural frequencies of the superstructure excited by the white noise and the 25 % seismic wave were comparable, indicating only minor damage. As the earthquake intensity increased, the natural frequencies of the first two modes were expected to decrease, which indicates more severe damage. The findings are consistent with the restoring forces shown in Fig. 11. Notably, as the load amplitude increased, the pole corresponding to the second mode became more prominent, facilitating its extraction. Therefore, the use of the first two natural frequencies makes this structural damage assessment more reliable.

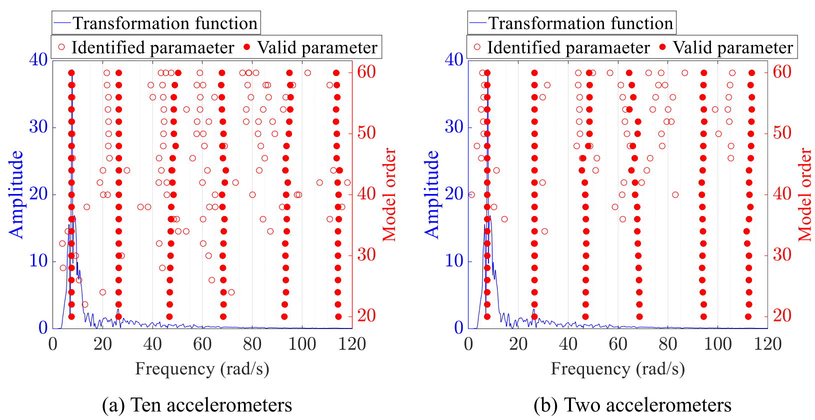

Fig. 12. Transformation function of the isolation layer and parameters identified by SI subjected to a 50 % earthquake wave.

Table 2
Natural frequencies identified by SI and transformation function.

Method	Order					
	First	Second	Third	Fourth	Fifth	Sixth
SI using 10 sensors (rad/s)	7.48	26.47	47.79	68.23	93.73	114.24
Transformation function (rad/s)	7.62	26.27	–	–	–	–
Relative error (%)	1.94	0.75	–	–	–	–

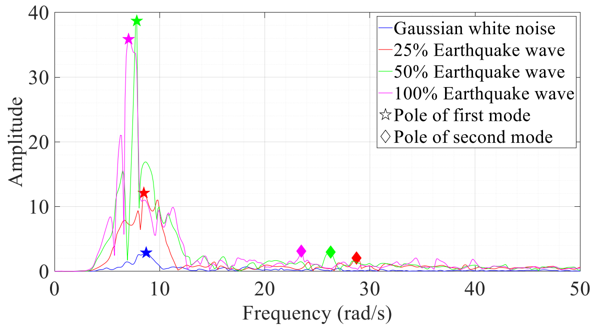

Fig. 13. Transformation function under different excitations.

4.3. Real-life base-isolated building

The proposed algorithm was applied to a base-isolated office building at the Hiyoshi campus of Keio University, Japan. Its superstructure was a concrete-filled steel tube frame structure of seven stories, reaching a height of 30.95 m. The isolation layer comprised three types of equipment: 6 oil dampers, 55 high-damping rubber bearings with diameters ranging from 750 to 900 mm, and 9 elastic sliding bearings. These energy dissipation and seismic isolation devices can reduce the extent of structural damage during earthquakes. A sensing system was deployed to monitor the structural status. As shown in Fig. 14 and Table 3, totally 16 accelerometers at 7 places and 3 displacement meters at 2 places were installed in the building. In detail, #1 was located at the bottom of the isolation layer to measure the excitation of the structure, #2 and #3 were placed at the bottom of the superstructure (i.e., the top of the isolation story) to record the absolute acceleration of the base, #4 was located at the bottom of the fourth floor, and #5, #6, and #7 were installed on the top floor to detect the acceleration responses. The inter-story displacement was measured by sensors at #102 and #103.

The proposed modal identification method was validated using two earthquake waves. The structural responses to the two seismic inputs along the X direction were larger than that along the Y direction. Hence, the responses along the X direction recorded by the sensors at #2, #4, #5, and #102 were focused on. The building is regular, so the inter-story deformations can be considered approximately uniform. The time-history and power spectral density of the two seismic waves along the X direction are illustrated in Fig. 15. The first wave had a seismic intensity of 3 in Japanese standard. The maximum peak value along the X direction was 0.075 m/s^2, and the energy was in the range of 0–30 rad/s. The second seismic excitation had a seismic intensity of 5-; the peak value along the X direction reached 0.701 m/s^2, with an energy distribution in the range of 0–40 rad/s. Hysteresis loops were used to determine the status of the energy dissipation and seismic isolation devices. The mass of all the floors was obtained from the design documents, and the input at the bottom of the superstructure was measured. However, the contribution of the inertial force of each floor to the restoring force cannot be directly obtained, as only the responses of the two floors of the superstructure were recorded. To overcome this issue, the mode shape expansion was employed [34]. First, the mode shapes of the two floors with the sensors were identified. Then, the Guyan static expansion was recommended in this study due to its simplicity. Consequently, all the floor responses can be determined approximately by using modal coordinates. The restoring forces in the isolation layer of the structure subjected to the two earthquakes are shown in Fig. 16. The devices in the isolation layer behaved linearly under the first earthquake because of its minor amplitude, whereas hysteresis was observed under the second seismic wave. However, the hysteretic behavior of the first story in the superstructure could not be computed, as the responses of the bottom of the second story which are necessary to calculate the restoring forces of the first story were not measured.

The SI was applied to extract the natural frequency of the superstructure. The acceleration responses measured at #2 were considered the input, and the absolute responses at #4 and #5 were considered the output. In the case of earthquake 1 (Fig. 17 (a)), the parameters in the first two modes were identified, while the effectiveness of the identification for the higher modes was poor. When the building was subjected to an earthquake with a seismic intensity of 5-, as shown in Fig. 17 (b), the standard deviation of the valid parameters in the first two modes decreased as the amplitude of the loads increased; however, the parameter estimation for the higher modes remained challenging. In summary, only the first two modes of the real-life building were reliably identified by the SI, and the accuracy of the estimation improved with an increase in the seismic intensity of the earthquake. Furthermore, the transformation

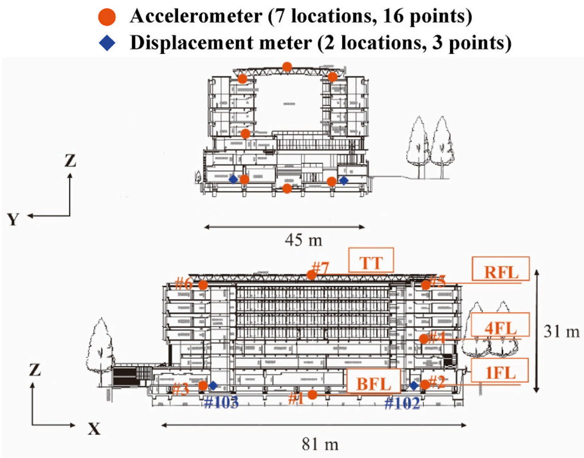

Fig. 14. Structural elevation views and sensor placement.

Table 3
Details of the sensing system.

Direction	X	Y	Z
Accelerometers	#1, #2, #4, #5	#1, #2, #3, #4, #5, #6	#1, #2, #3, #5, #6, #7
Displacement sensors	#102	#102, #103	

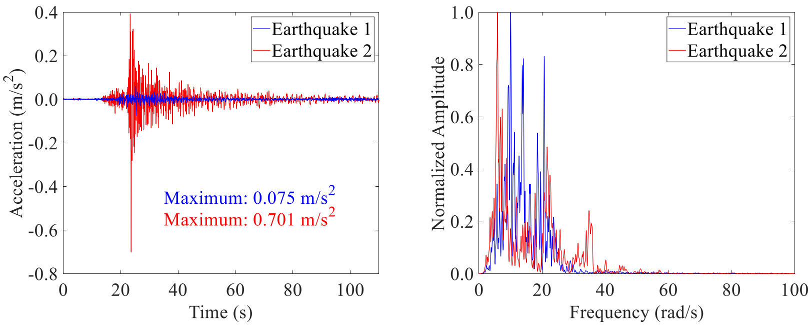

(a) Time history (b) Normalized power spectral density

Fig. 15. Two seismic waves along the X direction.

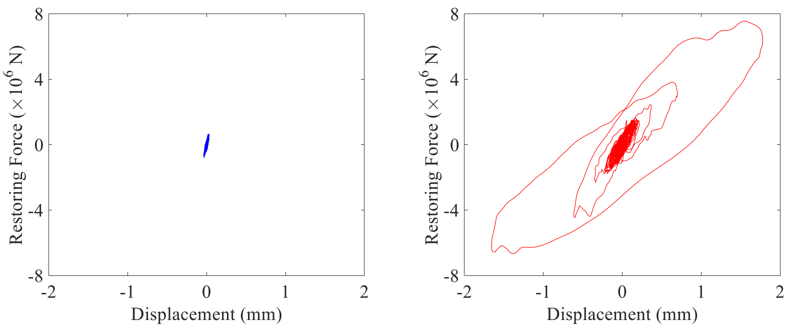

(a) Earthquake 1 (b) Earthquake 2

Fig. 16. Hysteretic curves of the isolation layer.

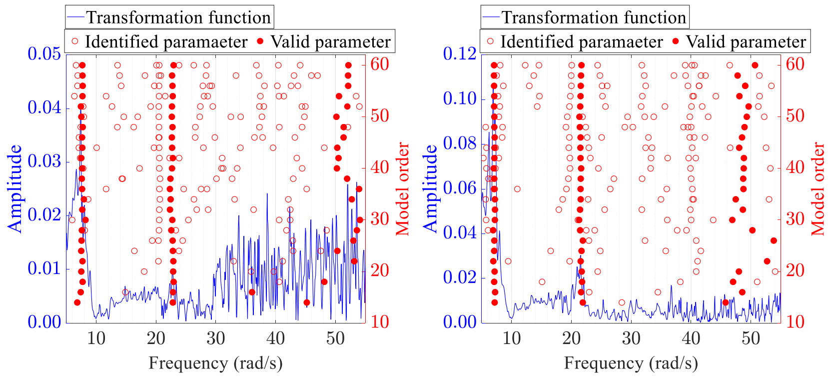

(a) Earthquake 1 (b) Earthquake 2

Fig. 17. Transformation function of the isolation story and parameters identified by SI.

function was computed using the measured inter-story displacement at #102 and acceleration at #2 which are plotted in Fig. 17. The pole corresponding to the first mode was prominent, whereas that of the second mode was inconspicuous in both cases. In addition, the parameter of the second mode of the superstructure under the earthquake 2 was easier to identify than that under the earthquake 1, presumably because the higher amplitude of the responses reduced the influence of noise. This phenomenon is consistent with the results of the E-Defense test. The natural frequencies of the first two modes identified by the SI and the transformation function with their relative errors are listed in Table 4. The errors in the first natural frequency were within 3 %, and the errors became minor for the second mode, indicating the applicability of the proposed method for modal identification. The natural frequencies of the first two modes for earthquake 2 were smaller than that for earthquake 1, indicating slight damage to the superstructure during earthquake 2.

4.4. Discussion

The proposed transforamtion function successfully identified the natural frequencies of the superstructure. When the whole structure behaved linearly and a sinusoidal sweep wave that covers all the modes of the superstructure was used for excitation, the poles corresponding to all the modes of the superstructure were clearly observed in the transformation function curve. However, in the cases of a full-scale structure and a real-life building experiencing an earthquake, the proposed method could identify only the first two modes. This could be attributed to the following reasons: (i) the frequency band of the earthquakes in a certain energy range does not fully cover all the modes; and (ii) the nonlinearity of the isolation system prevents the appearance of the poles of the higher modes of the superstructure. In particular, the peak of the first mode was pronounced, whereas the peak of the second mode was more easily identifiable with increasing earthquake intensity. The first two natural frequencies can indicate the presence of damage in a structure, while further damage localization and quantification require additional information [19]. It is worth noting that the observability of modal poles depends on the frequency variable. Compared to multi-story buildings, high-rise structures exhibit more modes within the same frequency range. As a result, the transformation function can extract more natural frequencies for high-rise buildings. For comparison, the SI was utilized. The SI accurately identified all the modal parameters of linear structures. Notably, higher-order modes of the superstructure under seismic excitation were identified in the E-Defense test; however, the estimation accuracy began to decline. In the case of a real-life building, SI identified only the first two modes, where the effectiveness depended on the amplitude of the external input. This is consistent with the transformation function-based identification. Overall, the results from SI and the transformation function were comparable. An interesting observation is that the relative errors of the identified parameters of the second mode are smaller than those of the first mode, but no clear theory supports this phenomenon. Moreover, when calculating the transformation function using the Fourier transform, the choice of window function types has little effect on the results. Although the assumption that the superstructure remains linear despite damage did not strictly hold, these time-invariant approaches accurately and reliably identified the different natural frequencies of the superstructure at varying levels of damage. In addition, the proposed algorithm could not extract the damping characteristics and mode shapes of the superstructure at this stage. However, the identification of the first two natural frequencies can provide crucial evidence of damage to the superstructure.

From the perspective of a sensing system, the transformation function can be determined from the acceleration and displacement

Table 4
Natural frequencies identified by the two methods.

	Earthquake 1 (Intensity 3)			Earthquake 1 (Intensity 5-)		
	SI (rad/s)	Transformation function (rad/s)	Relative error (%)	SI (rad/s)	Transformation function (rad/s)	Relative error (%)
First mode	7.64	7.42	2.94	7.10	6.92	2.65
Second mode	22.76	22.76	0.01	21.56	21.54	0.07

responses of the isolation layer. In other words, only an accelerometer and a displacement sensor installed at the top of the isolation layer are sufficient to calculate the transformation function. For instance, only the sensors at #2 and #102 in the real-life building were sufficient for modal identification. This is a significant result, as installing equipment on the same floor can reduce labor cost and expenditure. In contrast, at least two accelerometers on different floors and one sensor on the bottom of the superstructure were required for the SI method. For instance, the sensors at #2, #4, and #5 in the real-life building were required for modal identification. Hence, the sensing system for the SI method requires more space in the building and has higher installation and maintenance costs than those of the proposed method. Therefore, the proposed method can significantly simplify the monitoring system while ensuring the effectiveness of structural assessment.

5. Conclusion

In this study, we developed a novel modal identification algorithm for the superstructures of base-isolated buildings by using a transformation function. The transformation function can be computed by only the absolute acceleration and the inter-story drift of the isolation layer. This method requires only an accelerometer and a displacement sensor on the base (i.e., it does not require sensors on the superstructure), facilitating a simple and inexpensive monitoring system. The transformation function was initially developed using a substructural approach under linear conditions and then was extended to the more common nonlinear conditions using a generalized frequency response function. Subsequently, numerical simulations of a base-isolated structure were conducted using a Bouc-Wen hysteresis model to investigate the influence of the different degrees of nonlinearity. Next, the proposed algorithm was validated by applying it to three real-world examples: a scaled steel structure in the laboratory, a full-scale RC structure equipped with sliding bearings at the base, and a real-life base-isolated building equipped with bearings and dampers. Various column sizes were used to simulate the damage in the first case, and excitation loads with different amplitudes were investigated for the last two cases.

The main conclusions can be obtained by the results.

- The magnitude of the inter-story stiffness of the isolation layer had no impact on the position of the poles of the transformation function under linear conditions, and all the modes of the superstructure were accurately estimated by the proposed algorithm when these modes were sufficiently excited.
- When the isolation system exhibited nonlinearity, the extent of the nonlinearity did not change the horizontal coordinates of the poles of the superstructure.
- The peaks corresponding to the first two modes depended on the amplitude of the external load, whereas information on higher-order modes could not be determined from the function curves owing to the nonlinearity. The first two natural frequencies were accurately identified from the transformation function, regardless of the type of the devices installed on the isolation level.
- The identified natural frequencies of the base-isolated building varied with earthquakes of different intensities (i.e., the building experienced varying degrees of damage), even though the assumption that the superstructure exhibited linear behavior did not strictly hold.
- The results of the proposed method were consistent with that of the SI method, which confirms the effectiveness of the transformation function-based modal identification.

In the future, the following directions hold significant research value.

- The proposed method can be integrated with time-frequency analysis to monitor the real-time variations of the natural frequencies of the superstructure, providing more critical evidence for damage recognition.
- When the base-isolated building is irregular, the torsional modes play an important role on the structural assessment. In this case, multiple pairs of acceleration and displacement sensors can be placed on the control points, and the single-input, single-output transformation function can be extended to a multiple-input, multiple-output form for the identification of complex modes.
- The transformation function is derived under seismic loading, and thus, this method is not applicable to cases involving wind loads. The modal identification of the superstructure based on the transformation function under different types of loads requires further investigation.

CRediT authorship contribution statement

Kangqian Xu: Writing – original draft, Validation, Software, Methodology, Investigation, Formal analysis, Conceptualization, Data curation. **Miao Cao:** Writing – review & editing, Validation, Methodology, Funding acquisition, Data curation. **Songtao Xue:** Supervision, Methodology, Funding acquisition. **Xianzhi Li:** Writing – review & editing, Funding acquisition. **Jigang Zhang:** Supervision, Methodology. **Zhuoran Yi:** Writing – review & editing, Validation, Methodology, Investigation. **Liyu Xie:** Validation, Supervision.

Declaration of competing interest

The authors declare that they have no known competing financial interests or personal relationships that could have appeared to influence the work reported in this paper.

Acknowledgements

The authors would like to thank Editage (www.editage.cn) for English language editing. The experimental data of the full-scale RC structure used in this study was obtained from the E-Defense Experimental Data Archive (ASEBI) (https://doi.org/10.17598/nied.0020), project titled "Experimental Study on Collapse Mechanism of 10-story RC Frame Based on Current Seismic Design Code and Advanced High Seismic Technology" conducted at the National Research Institute for Earth Science and Disaster Resilience of Japan. This study was partially supported by grants from the Japan Society for the Promotion of Science (JSPS) (Kakenhi No. 18K04438), the Tohoku Institute of Technology Research Grant (No. 2024-05), and the National Natural Science Foundation of China (No. 52408339).

Data availability

The authors do not have permission to share data.

References

[1] R. Jangid, Stochastic response of building frames isolated by lead–rubber bearings, Struct. Control Health Monit.: The Official Journal of the International Association for Structural Control and Monitoring and of the European Association for the Control of Structures 17 (2010) 1–22, https://doi.org/10.1002/stc.266.

[2] C. Li, K. Chang, L. Cao, Y. Huang, Performance of a nonlinear hybrid base isolation system under the ground motions, Soil Dynam. Earthq. Eng. 143 (2021) 106589, https://doi.org/10.1016/j.soildyn.2021.106589.

[3] O.P. Maksymenko, O.M. Sakharuk, Y.L. Ivanytskyi, P.S. Kun, Multilaser spot tracking technology for bridge structure displacement measuring, Struct. Control Health Monit. 28 (2021) e2675, https://doi.org/10.1002/stc.2675.

[4] C. Sun, D. Gu, X. Lu, Three-dimensional structural displacement measurement using monocular vision and deep learning based pose estimation, Mech. Syst. Signal Process. 190 (2023) 110141, https://doi.org/10.1016/j.ymssp.2023.110141.

[5] X. Ye, S. Ma, Z. Liu, Y. Ding, Z. Li, T. Jin, Post-earthquake damage recognition and condition assessment of bridges using UAV integrated with deep learning approach, Struct. Control Health Monit. 29 (2022) e3128, https://doi.org/10.1002/stc.3128.

[6] N. Murota, S. Suzuki, T. Mori, K. Wakishima, B. Sadan, C. Tuzun, et al., Performance of high-damping rubber bearings for seismic isolation of residential buildings in Turkey, Soil Dynam. Earthq. Eng. 143 (2021) 106620, https://doi.org/10.1016/j.soildyn.2021.106620.

[7] S. Narasimhan, S. Nagarajaiah, E.A. Johnson, H.P. Gavin, Smart base-isolated benchmark building. Part I: problem definition, Struct. Control Health Monit.: The Official Journal of the International Association for Structural Control and Monitoring and of the European Association for the Control of Structures 13 (2006) 573–588, https://doi.org/10.1002/stc.99.

[8] J. Kang, Z. Zhao, L. Xie, C. Wan, S. Xue, Proportional distribution pattern and modal principle of tuned viscous mass dampers for multi-degree-of-freedom structures, Eng. Struct. 322 (2025) 119175, https://doi.org/10.1016/j.engstruct.2024.119175.

[9] J. Kang, K. Ikago, Seismic control of multidegree-of-freedom structures using a concentratedly arranged tuned viscous mass damper, Earthq. Eng. Struct. Dynam. 52 (2023) 4708–4732, https://doi.org/10.1002/eqe.3977.

[10] L. Cao, X. Li, Y. Huang, C. Li, H. Pan, High robust eddy current tuned tandem mass dampers-inerters for structures under the ground acceleration, Soil Dynam. Earthq. Eng. 188 (2025) 109040, https://doi.org/10.1016/j.soildyn.2024.109040.

[11] L. Wang, S. Nagarajaiah, Y. Zhou, W. Shi, Experimental study on adaptive-passive tuned mass damper with variable stiffness for vertical human-induced vibration control, Eng. Struct. 280 (2023) 115714, https://doi.org/10.1016/j.engstruct.2023.115714.

[12] X. Chen, D. De Domenico, L. Chunxiang, Seismic resilient design of rocking tall bridge piers using inerter-based systems, Eng. Struct. 281 (2023) 115819, https://doi.org/10.1016/j.engstruct.2023.115819.

[13] L. Wang, Y. Zhou, W. Shi, Seismic response control of a nonlinear tall building under mainshock–aftershock sequences using semi-active tuned mass damper, Int. J. Struct. Stabil. Dynam. 23 (2023) 2340027, https://doi.org/10.1142/S0219455423400278.

[14] L. Wang, S. Nagarajaiah, W. Shi, Y. Zhou, Seismic performance improvement of base-isolated structures using a semi-active tuned mass damper, Eng. Struct. 271 (2022) 114963, https://doi.org/10.1016/j.engstruct.2022.114963.

[15] Y. Chen, D. Sato, K. Miyamoto, J. She, Response-spectrum-based design method for active base-isolated buildings with viscous dampers and hysteretic dampers, Mech. Syst. Signal Process. 180 (2022) 109413, https://doi.org/10.1016/j.ymssp.2022.109413.

[16] P. Chen, P. Chen, G. Ting, Seismic response mitigation of buildings with an active inerter damper system, Struct. Control Health Monit. 29 (2022) e2975, https://doi.org/10.1002/stc.2975.

[17] K. Kasai, A. Mita, H. Kitamura, K. Matsuda, T.A. Morgan, A.W. Taylor, Performance of seismic protection technologies during the 2011 Tohoku-Oki earthquake, Earthq. Spectra 29 (2013) 265–293, https://doi.org/10.1193/1.4000131.

[18] F. Hernández, P. Díaz, R. Astroza, F. Ochoa-Cornejo, X. Zhang, Time variant system identification of superstructures of base-isolated buildings, Eng. Struct. 246 (2021) 112697, https://doi.org/10.1016/j.engstruct.2021.112697.

[19] V.R. Gharehbaghi, E. Noroozinejad Farsangi, M. Noori, T. Yang, S. Li, A. Nguyen, et al., A critical review on structural health monitoring: definitions, methods, and perspectives, Arch. Comput. Methods Eng. (2021) 1–27, https://doi.org/10.1007/s11831-021-09665-9.

[20] O. Avci, O. Abdeljaber, S. Kiranyaz, M. Hussein, M. Gabbouj, D.J. Inman, A review of vibration-based damage detection in civil structures: from traditional methods to Machine Learning and Deep Learning applications, Mech. Syst. Signal Process. 147 (2021) 107077, https://doi.org/10.1016/j.ymssp.2020.107077.

[21] X. Kong, C.-S. Cai, J. Hu, The state-of-the-art on framework of vibration-based structural damage identification for decision making, Appl. Sci. 7 (2017) 497, https://doi.org/10.3390/app7050497.

[22] B. Bhowmik, T. Tripura, B. Hazra, V. Pakrashi, Real time structural modal identification using recursive canonical correlation analysis and application towards online structural damage detection, J. Sound Vib. 468 (2020) 115101, https://doi.org/10.1016/j.jsv.2019.115101.

[23] M. Mishra, P.B. Lourenço, G.V. Ramana, Structural health monitoring of civil engineering structures by using the internet of things: a review, J. Build. Eng. 48 (2022) 103954, https://doi.org/10.1016/j.jobe.2021.103954.

[24] A. Khan, S. Gupta, S.K. Gupta, Multi-hazard disaster studies: monitoring, detection, recovery, and management, based on emerging technologies and optimal techniques, Int. J. Disaster Risk Reduc. 47 (2020) 101642, https://doi.org/10.1016/j.ijdrr.2020.101642.

[25] P.K. Paul, A. Dutta, S.K. Deb, Comparison of the performance of nonlinear Kalman filter based algorithms for state-parameter identification of base isolated structures, Struct. Control Health Monit. 29 (2022) e3029, https://doi.org/10.1002/stc.3029.

[26] R. Astroza, J.P. Conte, J.I. Restrepo, H. Ebrahimian, T. Hutchinson, Seismic response analysis and modal identification of a full-scale five-story base-isolated building tested on the NEES@ UCSD shake table, Eng. Struct. 238 (2021) 112087, https://doi.org/10.1016/j.engstruct.2021.112087.

[27] R. Astroza, G. Gutiérrez, C. Repenning, F. Hernández, Time-variant modal parameters and response behavior of a base-isolated building tested on a shake table, Earthq. Spectra 34 (2018) 121–143, https://doi.org/10.1193/032817EQS054M.

[28] M. Dan, Y. Ishizawa, S. Tanaka, S. Nakahara, S. Wakayama, M. Kohiyama, Vibration characteristics change of a base-isolated building with semi-active dampers before, during, and after the 2011 Great East Japan earthquake, Earthquakes and Structures 8 (2015) 889–913, https://doi.org/10.12989/eas.2015.8.4.889.

[29] S. Nagarajaiah, S. Xiaohong, Response of base-isolated USC hospital building in Northridge earthquake, J. Struct. Eng. 126 (2000) 1177–1186, https://doi.org/10.1061/(ASCE)0733-9445(2000)126:101177.

[30] X. Chen, T. Yang, W. Shi, Influence of isolation hysteresis on the seismic performance of isolated buildings, Struct. Control Health Monit. 22 (2015) 631–647, https://doi.org/10.1002/stc.1709.
[31] R.S. Jangid, Performance and optimal design of base-isolated structures with clutching inerter damper, Struct. Control Health Monit. 29 (2022) e3000, https://doi.org/10.1002/stc.3000.
[32] P.T. Brewick, E.A. Johnson, E. Sato, T. Sasaki, Constructing and evaluating generalized models for a base-isolated structure, Struct. Control Health Monit. 25 (2018) e2243, https://doi.org/10.1002/stc.2243.
[33] D.M. Siringoringo, Y. Fujino, Seismic response analyses of an asymmetric base-isolated building during the 2011 Great East Japan (Tohoku) Earthquake, Struct. Control Health Monit. 22 (2015) 71–90, https://doi.org/10.1002/stc.1661.
[34] L. Xie, A. Mita, Using component mode synthesis to estimate the restoring force of an isolation layer subjected to earthquakes, Struct. Control Health Monit.: The Official Journal of the International Association for Structural Control and Monitoring and of the European Association for the Control of Structures 17 (2010) 152–177, https://doi.org/10.1002/stc.281.
[35] M.L. Ivanov, W.-K. Chow, Structural Damage Observed in Reinforced Concrete Buildings in Adiyaman during the 2023 Turkiye Kahramanmaras Earthquakes, vol. 58, Elsevier, 2023 105578, https://doi.org/10.1016/j.istruc.2023.105578.
[36] E. Tapia-Hernández, J.S. García-Carrera, Damage assessment and seismic behavior of steel buildings during the Mexico earthquake of 19 September 2017, Earthq. Spectra 36 (2020) 250–270, https://doi.org/10.1177/8755293019878186.
[37] X. Zhang, J. He, X. Hua, Z. Chen, Z. Feng, Simultaneous identification of time-varying parameters and external loads based on extended kalman filter: approach and validation, Struct. Control Health Monit. 2023 (2023) 8379183, https://doi.org/10.1155/2023/8379183.
[38] K. Huang, K.-V. Yuen, L. Wang, Real-time simultaneous input-state-parameter estimation with modulated colored noise excitation, Mech. Syst. Signal Process. 165 (2022) 108378, https://doi.org/10.1016/j.ymssp.2021.108378.
[39] J.N. Yang, S. Lin, H. Huang, L. Zhou, An adaptive extended Kalman filter for structural damage identification, Struct. Control Health Monit.: The Official Journal of the International Association for Structural Control and Monitoring and of the European Association for the Control of Structures 13 (2006) 849–867, https://doi.org/10.1002/stc.84.
[40] Y. Zhou, X. Luo, W. Zhang, P. Ye, J. Chen, Z. Du, Improvement of axial deformation prediction in high-rise buildings with field monitoring and adaptive unscented Kalman filter, J. Build. Eng. 83 (2024) 108432, https://doi.org/10.1016/j.jobe.2023.108432.
[41] T. Yu, Z. Wang, J. Wang, An iterative augmented unscented Kalman filter for simultaneous state-parameter-input estimation for systems with/without direct feedthrough, Mech. Syst. Signal Process. 205 (2023) 110793, https://doi.org/10.1016/j.ymssp.2023.110793.
[42] E.A. Wan, R. Van Der Merwe, The unscented Kalman filter for nonlinear estimation, Ieee (2000) 153–158, https://doi.org/10.1109/ASSPCC.2000.882463.
[43] V. Ondra, I. Sever, C. Schwingshackl, Identification of complex non-linear modes of mechanical systems using the Hilbert-Huang transform from free decay responses, J. Sound Vib. 495 (2021) 115912, https://doi.org/10.1016/j.jsv.2020.115912.
[44] S. Li, J.-W. Pan, G.-H. Luo, J.-T. Wang, Improvements in the HHT for the modal parameter identification of structures with closely spaced modes, J. Earthq. Eng. 26 (2022) 331–356, https://doi.org/10.1080/13632469.2019.1686091.
[45] R. Janeliukstis, Continuous wavelet transform-based method for enhancing estimation of wind turbine blade natural frequencies and damping for machine learning purposes, Measurement 172 (2021) 108897, https://doi.org/10.1016/j.measurement.2020.108897.
[46] Y. Kankanamge, Y. Hu, X. Shao, Application of wavelet transform in structural health monitoring, Earthq. Eng. Eng. Vib. 19 (2020) 515–532, https://doi.org/10.1007/s11803-020-0576-8.
[47] Tosauchi Y, Sato E, Fukuyama K, Inoue T, Kajiwara K, Shiohara H, et al. 2015 Three-Dimensional Shaking Table Test of a 10-story Reinforced Concrete Building on the E-Defense n.d.
[48] P. Brewick, W.M. Elhaddad, E.A. Johnson, T. Abrahamsson, E. Sato, T. Sasaki, Hybrid Time/Frequency Domain Identification of Real Base-Isolated Structure, Springer, 2016, pp. 303–311, https://doi.org/10.1007/978-3-319-29751-4_31.
[49] R. Yoshimoto, A. Mita, K. Okada, Damage detection of base-isolated buildings using multi-input multi-output subspace identification, Earthq. Eng. Struct. Dynam. 34 (2005) 307–324, https://doi.org/10.1002/eqe.435.
[50] W. Yan, W. Ren, Operational modal parameter identification from power spectrum density transmissibility, Comput. Aided Civ. Infrastruct. Eng. 27 (2012) 202–217, https://doi.org/10.1111/j.1467-8667.2011.00735.x.
[51] K. Xu, A. Mita, D. Li, S. Xue, X. Li, A Constrained Minimization-Based Scheme against Susceptibility of Drift Angle Identification to Parameters Estimation Error from Measurements of One Floor, vol. 33, 2024, pp. 119–131, https://doi.org/10.12989/sss.2024.33.2.119.
[52] K. Xu, M. Cao, S. Xue, D. Li, X. Li, Z. Yi, Single accelerometer-based inter-story drift reconstruction of soft-story for shear structures with innovative transformation function, Mech. Syst. Signal Process. 222 (2025) 111800, https://doi.org/10.1016/j.ymssp.2024.111800.
[53] C. Cheng, Z. Peng, W. Zhang, G. Meng, Volterra-series-based nonlinear system modeling and its engineering applications: a state-of-the-art review, Mech. Syst. Signal Process. 87 (2017) 340–364, https://doi.org/10.1016/j.ymssp.2016.10.029.
[54] A. Chatterjee, H.P. Chintha, Identification and parameter estimation of cubic nonlinear damping using harmonic probing and volterra series, Int. J. Non Lin. Mech. 125 (2020) 103518.
[55] R. de O. Teloli, S. da Silva, A new way for harmonic probing of hysteretic systems through nonlinear smooth operators, Mech. Syst. Signal Process. 121 (2019) 856–875.
[56] T.T. Baber, M.N. Noori, Modeling general hysteresis behavior and random vibration application. https://doi.org/10.1115/1.3269364, 1986.
[57] M. Lin, C. Cheng, G. Zhang, B. Zhao, Z. Peng, G. Meng, Identification of Bouc-Wen hysteretic systems based on a joint optimization approach, Mech. Syst. Signal Process. 180 (2022) 109404, https://doi.org/10.1016/j.ymssp.2022.109404.
[58] P. Van Overschee, B. De Moor, Subspace Identification for Linear Systems: Theory—Implementation—Applications, Springer Science & Business Media, 2012.